Microstructural interactions contribute to the hotspot in the living cochlea

Junpei Liu[1,3#], Yanru Bai[1,3#], Qianli Cheng[2], Shu Zheng[1,3], Stephen Elliott[4]* and Guangjian Ni[1,2,3]*

[1] Academy of Medical Engineering and Translational Medicine, Tianjin University, Tianjin, 300072 China

[2] Department of Biomedical Engineering, College of Precision Instruments and Optoelectronics Engineering, Tianjin University, Tianjin, 300072 China

[3] Tianjin Key Laboratory of Brain Science and Neuroengineering, Tianjin, 300072 China

[4] Institute of Sound and Vibration Research, University of Southampton, Southampton, SO17 1BJ UK

[#] contributed equally to this work

[*] Correspondence should be addressed to Stephen J Elliott: S.J.Elliott@soton.ac.uk and Guangjian Ni: niguangjian@tju.edu.cn

Highlights:

- 3D cochlea segmental models including micro-physiological structures were developed.
- The hotspot vibration is a local phenomenon in the cochlea.
- The hotspot appears in the high- and low-frequency regions in the cochlea.

Abstract

The mechanism of the active cochlea relies on a complex interaction between microstructures in the organ of Corti. A significant longitudinal vibration "hotspot" was

recently observed in the high-frequency region of the living gerbil cochlea between the Deiters cells and the outer hair cells. A similar phenomenon was also found in guinea pigs with a relatively smaller magnitude. The cause is unknown, but one hypothesis is that this phenomenon is due to the structural constraints between different microstructures. It is not easy to explain the mechanism of hotspots directly from experimental observations. It may also be difficult to image or test if the hotspot will occur in the low-frequency region in the cochlea. We built two three-dimensional finite element models corresponding to the high- and low-frequency regions in the guinea pig cochlea. Responses of the organ of Corti to passive acoustic and outer hair cell electrical excitation were calculated. The two excitations were then superimposed to predict the active response of the organ of Corti. The hotspot phenomenon in the experiment was reproduced and analyzed in-depth about influencing factors. Our results indicate that hotspots appear in the low-frequency region of the cochlea as well. We hypothesize that the hotspot is a locally originated phenomenon in the cochlea, and the traveling wave further enhances the response to low-frequency excitation. The movement of outer hair cells inclined in the longitudinal direction is the leading cause of the hotspot.

Keywords: Hotspot, organ of Corti, finite element model, low-frequency

1 Introduction

The active amplification mechanism of the cochlea is related to the microscopic movement in the organ of Corti (OC) (Robles and Ruggero, 2001; von Bekesy, 1970). At present, our understanding of this mechanism mainly relies on measurements in animal experiments. Attention has been paid to the transverse movement of the basilar membrane (BM), reticular lamina (RL), and tectorial membrane (TM), and differences in the amplitude and phase were found (He et al., 2018; Ren et al., 2016). Recent experiments have started to explore the areas of Deiters cells (DCs) and outer hair cells (OHCs) (Cooper et al., 2018). They found that in the high-frequency region of the living gerbil cochlea, the longitudinal response is significant and even greater than that of the basilar membrane. This response is most evident near the connection between OHCs and DCs, called "hotspot". Similarly, Fallah et al. (2021) found that hotspot responses also occur in the guinea pig, but the response magnitude was smaller than the gerbil.

57 Cooper et al. (2018) proposed that this phenomenon is driven by the movement of
58 OHCs, under the structural constraints of the organ of Corti. According to their
59 hypothesis, a similar response may also occur in the low-frequency region of the
60 cochlea, although this has not been observed experimentally yet.

61 This paper studied the hotspot using three-dimensional segmental finite element models
62 of the cochlea. Such models could reproduce experimentally observed results and test
63 different hypotheses. Our work showed that the hotspot could be simulated under the
64 following conditions:

65   (1) Including a three-dimensional structure that can simulate longitudinal
66 movement.
67   (2) Including the Phalangeal process (PhPs) to form a longitudinal structural
68 constraint.
69   (3) Including the physiological details of the organ of Corti to form a strong
70 constraint between microstructures.
71   (4) Ability to simulate the active response of the cochlea.

72 However, most of the existing cochlear models cannot meet the above conditions.
73 Traditional two-dimensional models cannot simulate the longitudinal movement of the
74 organ of Corti (Cai and Chadwick, 2003; Cai et al., 2004; Ni et al., 2016; Steele and
75 Puria, 2005). Beam models always need to simplify the geometry of the organ of Corti
76 (Nam, 2014; Nam and Fettiplace, 2010), but three-dimensional models could reflect
77 more detailed physiological structures (Zagadou et al., 2020). The "feedforward"
78 models proposed by Steele et al. (1993, 1999) and Geisler et al. (1995) reproduced
79 many of the structural features but did not focus on producing the longitudinal vibration
80 in the hotspot.

81 In this paper, we developed two three-dimensional segmented cochlear models,
82 including detailed micro-physiological structures in the organ of Corti, corresponding
83 to cochlear high- and low-frequency regions, respectively. These models included
84 orthotropic material properties of some microstructures, the OHCs longitudinal tilt, the
85 PhPs, and the longitudinal coupling between discontinuous structures. The
86 superposition of the OC responses due to acoustic and OHCs excitation was used for
87 calculating the active cochlear responses. The hotspot results simulated by the high-

88   frequency model are compared with the experiments to verify the effectiveness. Similar

89   results were obtained using the low-frequency model. Further, we analyzed the effect

90   of viewing angle on the results. We then changed part of the excitation conditions and

91   structure settings to illustrate the role and influence of some factors on the hotspot

92   phenomenon.

2 Materials and methods

2. 1 Model overview

95   Two three-dimensional guinea pig cochlea segmental models were built in COMSOL

96   Multiphysics 5.6, including the detailed micro-physiological structures corresponding

97   to cochlear low- and high-frequency regions, as shown in Figure 1. The finite element

98   method was used to deal with the complexity of the geometric structures in the cochlea.

99   The models were built on the millimeter scale, and microstructures were on the

100 micrometer scale.

101 The high-frequency model was drawn based on geometry data from Salt laboratory[1]

102 corresponding to the position where the characteristic frequency is about 16 kHz, and

103 the total thickness is 36 μm. The low-frequency model was drawn based on the existing

104 two-dimensional model (Ni et al., 2016), corresponding to the position where the

105 characteristic frequency is 0.8 kHz and the total thickness is 60 μm.

106 First, we constructed a high-frequency model to reproduce the hotspot phenomenon in

107 the experiments. The measured region by Cooper et al. (2018) corresponds to

108 characteristic frequencies from about 20 kHz to 40 kHz. According to the gerbil cochlea

109 frequency tonotopy (Muller, 1996), this frequency range corresponds to a position

110 range 10% to 23% of the total gerbil cochlea length away from the base. For the guinea

111 pig cochlea, 10% to 23% of the total length away from the base corresponds to a

112 characteristic frequency range of 14.3 kHz to 27 kHz (Greenwood, 1990; Ni et al., 2017;

113 Nuttall et al., 1999). Therefore, we built our high-frequency model with a characteristic

114 frequency of 16 kHz. Referring to the data of Salt laboratory and Fernandez (Fernandez,

115 1952), the scala vestibuli (SV) height was 463 μm, the scala media (SM) height was 77

116 μm, the scala tympani (ST) width was 318 μm, and the BM width was 110 μm in the

117   high-frequency model. The average length of OHCs in the 16 kHz model was 23 μm,

118   consistent with estimations (Kelly, 1989).

119   Then we built the low-frequency model based on the 2D model by Ni et al. (2016). The

120   longitudinal continuity of microstructures in the cochlea was treated differently in the

121   model, as listed in Table 1. The scala fluid and part of the solid structures are

122   continuously distributed (Kikuchi et al., 1995). They were stretched with the same

123   length along the longitudinal direction as the overall model, 60 μm. A Thermoviscous-

124   Acoustics condition, used to solve linearized Navier–Stokes and Fourier heat equations,

125   was set for the fluids, but heat transmission was neglected, and only the fluid-flow

126   equations of momentum in the frequency domain were considered here, as

$$i\omega\rho_f \mathbf{u}_f = \nabla\cdot[-p_{\mathrm{va}}\mathbf{I} + \mu(\nabla\mathbf{u}_f + (\nabla\mathbf{u}_f)^{\mathrm{T}}) + (\mu_{\mathrm{B}} - \tfrac{2}{3}\mu)(\nabla\cdot\mathbf{u}_f)\mathbf{I}\,] = 0, \quad (1)$$

127   where $\mathbf{u}_f$ is the velocity field (the effects of gravity are neglected), ρ_f and p_f are the

128   fluid density and viscoacoustic fluid pressure. μ and μ_{B} are the dynamic and bulk

129   viscosity, respectively. $\mathbf{I}$ represents the unity matrix, and i, ∇, and ω are the imaginary

130   unit, differential operator, and angular frequency, respectively.

131   The pillar cells, hair cells, stereocilia, DCs, and Deiters rods were arranged at a specific

132   interval along the longitudinal direction (Raphael and Altschuler, 2003). The pillar and

133   hair cells were approximated as cylinders in the *y-z* plane with thickness of 3.2 μm and

134   8.4 μm in the longitudinal direction (Karavitaki and Mountain, 2007). The outer hair

135   cells were set to be inclined 10˚ in the longitudinal direction, referring to the average

136   measurement mice (Soons et al., 2015) because the guinea pig value is unknown yet.

137   The influence of different OHCs tilt angles on the results was discussed. The Deiters

138   cells were assigned the same longitudinal thickness with the outer hair cells, which were

139   close to measurement (Karavitaki and Mountain, 2007). The W or V-shaped hair

140   bundles at the top of the hair cells were simplified into the tallest row of stereocilia.

141   The stereocilia of OHCs were connected to the TM bottom, while the stereocilia of

142   IHCs were not (Lim, 1986). The stereocilia were all constructed with Timoshenko

143   beams and located in the middle layer of each segment along the longitudinal direction.

144   The diameters of the stereocilia, the PhPs, and the DC rods were set to be 0.2 μm, 1 μm,

145   and 1 μm, respectively (Bohnke et al., 1999; Nam and Fettiplace, 2010). The gaps

146 between the discontinuous structures were filled with fluid, and discontinuous
147 structures were entirely wrapped by fluid.

148 The PhPs were modeled with beam element, and one end was connected to the bottom
149 of OHCs, and the top of Deiters rods, forming a Y-shaped structure. The other end of
150 the PhPs was connected to the bottom of the reticular lamina. The average length of
151 OHCs in the 0.8 kHz model is about 45 μm, consistent with estimations (Kelly, 1989).
152 The experimental results show that the angle of OHCs and PhPs in the guinea pig
153 cochlea is about 35° (Zetes et al., 2012). Based on the trigonometric relationship
154 between the structures, the longitudinal spacing of PhPs is about 3 OHCs.

155

156 **Table 1** Continuity in the models

Components (abbreviation)	Continuity	Components (abbreviation)	Continuity
Scala vestibuli (SV)	Yes	Hensen stripe	Yes
Scala media (SM)	Yes	Pillar cell head (PC)	Yes
Scala tympani (ST)	Yes	Outer pillar cell (OPC)	No
Spiral ligament	Yes	Inner pillar cell (IPC)	No
Spiral lamina (SLa)	Yes	Inner hair cell (IHC)	No
Spiral limbus	Yes	Outer hair cell (OHC)	No
Inner sulcus cells (ISC)	Yes	Stereocilia (St)	No
Tectorial membrane (TM)	Yes	Deiters cell (DC)	No
Reticular lamina (RL)	Yes	Deiters cell rod (DC rod)	No
Basilar membrane (BM)	Yes	Phalangeal processes (PhPs)	No
Hensen cell (HenC)	Yes		

157
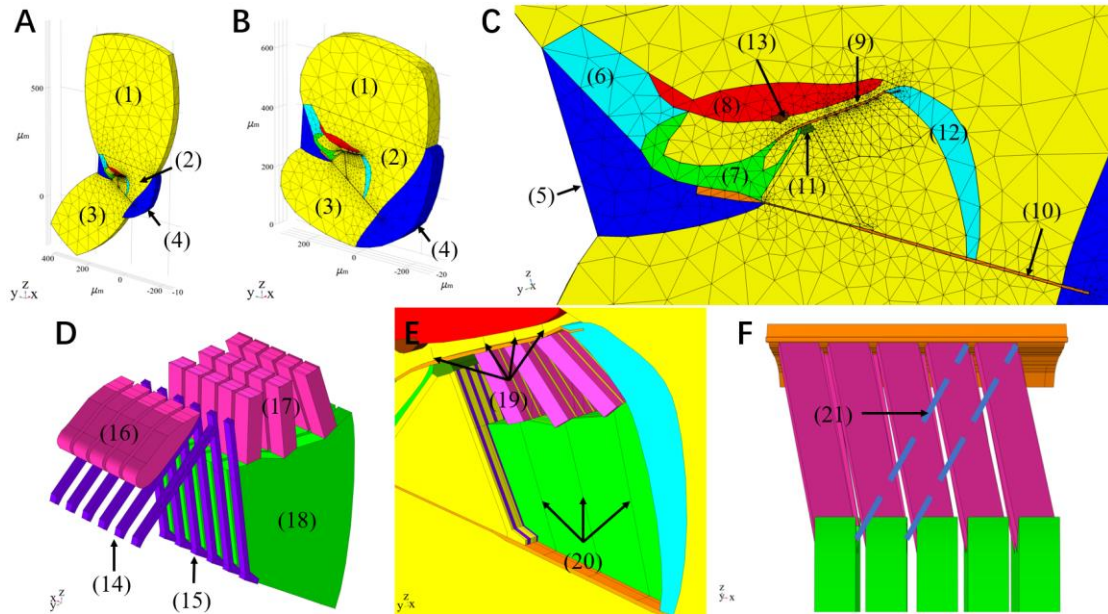
Figure 1: Three-dimensional segmental models of the guinea pig cochlea. (A) The high-frequency model with a CF of 16 kHz. (B) The low-frequency model with a CF of 0.8 kHz. (C) Structure and mesh of the organ of Corti. (D) Discontinuous components in the organ of Corti. (E) Beam structures of some discontinuous components in the organ of Corti. (F) PhPs span 3 outer hair cells longitudinally. All structure names included in the model are numbered as follow: (1) Scala vestibuli, (2) Scala media, (3) Scala tympani, (4) Spiral ligament, (5) Spiral lamina, (6) Spiral limbus, (7) Inner sulcus cells, (8) Tectorial membrane, (9) Reticular lamina, (10) Basilar membrane, (11) Pillar cell head, (12) Hensen cells, (13) Hensen stripe, (14) Inter pillar cells, (15) Outer pillar cells, (16) Inter hair cells, (17) Outer hair cells, (18) Deiters cells, (19) Stereocilia, (20) Deiters rods, (21) Phalangeal processes. Yellow segments denote fluid elements, black and blue lines denote beam elements, and the rest denote solid elastic elements.

2.2 Boundary conditions

In this work, both models used the same boundary conditions. The two ends of the basilar membrane were connected with the spiral lamina and the spiral ligament. The boundary conditions are more complicated and depend on the adjacent tissue and fiber structure. Ni et al. (2013) showed that boundary conditions at both ends of the basilar membrane have little effect on the fluid coupling and coupled response. Therefore, we fixed the spiral ligament and spiral lamina, corresponding to the tightening of the basilar membrane on both ends, which is consistent with Steele and Puria (2005) and Ni et al. (2016).

The solid surface was set as a continuous periodic condition to simulate their movement

180　under a periodic arrangement. This boundary condition makes the displacement of the

181　two sides of the boundary always equal, as,

$$u(x_\mathrm{d}) = u(x_\mathrm{s}), \tag{2}$$

182　where u is the displacement of solid, x_d and x_s are corresponding positions on both sides

183　of the model. The effect of this boundary condition was discussed in Appendix I. The

184　fluid was set to be no-stress boundary so that the total surface stress was zero, as,

$$[-p_t\mathbf{I}+\mu(\triangledown\mathbf{u_t}+(\triangledown\mathbf{u_t})^\mathrm{T})-(\frac{2\mu}{3}-\mu_\mathrm{B})(\triangledown\mathbf{u_t})\mathbf{I}]\mathbf{n}=0, \tag{3}$$

185　where p_t is the total acoustic pressure, $\mathbf{u}_\mathrm{t}$ is the total acoustic velocity, μ is the dynamic

186　viscosity, μ_B is the bulk viscosity, $\mathbf{I}$ is the second-order identity tensor, and $\mathbf{n}$ is the

187　normal direction. The no-stress boundary condition can simulate the longitudinal

188　pressure release of the fluid when the organ of Corti moves. For example, when the

189　organ of Corti moves, the volume of fluid in the SV and ST will change, which will

190　change the pressure. If there were no such setting, this pressure change would restrict

191　the movement of the organ of Corti. The effects of this boundary condition are

192　discussed in Appendix II.

193　All contact surfaces between fluid and solid in the models were set as Thermoviscous

194　Acoustic-Structure Boundary, which includes the coupling between the discontinuous

195　structure and the fluid inside the organ of Corti. This coupling is described in the

196　frequency domain as,

$$u_\mathrm{t,fluid} = i\omega u_\mathrm{solid} \tag{4}$$

197　where $u_\mathrm{t,fluid}$ is the total fluid velocity, and u_solid is the solid displacement. This coupling

198　ensures stress being continuous across the fluid-structure interface. Spatial continuity

199　of displacement is enforced at the connection nodes between the beam and solid

200　elements by,

$$\mathbf{u}_b = \mathbf{u}_s, \tag{5}$$

201　where $\mathbf{u}_b$ and $\mathbf{u}_s$ are the displacement of beam and solid, respectively. Since the beam

202　elements in finite element models do not feature actual surfaces to interact with the

203   surrounding domain, fluid–structure interaction conditions do not apply to beams.

204   **2.3 Material properties**

205   Material properties of each structure are listed in Table 2 and Table 3. To adjust the
206   resonance frequency to be consistent with the defined characteristic frequency, the
207   stiffness of some components was adjusted to be consistent with measurements and
208   existed models (Cai and Chadwick, 2003; Steele and Puria, 2005; Zwislocki and
209   Cefaratti, 1989)

210   Orthotropic materials were used for TM, RL, and BM. Liu et al. (2008) showed that the
211   orthotropy ratio was 10 at the upper-middle turn of the cochlea and 68 at the base. They
212   pointed out that the value may vary along the length of the cochlea. The guinea pig
213   cochlea was 18.5 mm long, and the characteristic frequency at the base, f_B, was 44 kHz
214   (Fernandez, 1952). The characteristic frequency of the guinea pig cochlea exponentially
215   decreases from the base to the apex (Greenwood, 1990; Nuttall et al., 1999), as

$$CF(x) = f_B\, e^{-x/l} \,, \tag{6}$$

216   where x is the distance to the base, and l is the characteristic frequency distribution
217   scale, which was set to 3.8 mm in our work. The location with a characteristic frequency
218   of 0.8 kHz was then calculated to be about 15.2 mm away from the base, close to the
219   cochlea upper-middle turn. Meanwhile, the 16 kHz position is 3.8 mm away from the
220   base. Therefore, the orthotropy ratio was set to 10 for the low-frequency model and 40
221   for the high-frequency model.

222   The density of all components in the model was the same as water, 1000 kg/m^3.
223   Poisson's ratio, v, had a linear relationship with Young's modulus, E, as $v=1/2-E/6/K$,
224   where K=1 GPa. The damping was included in the stiffness matrix as a loss factor of
225   0.1. The fluid was incompressible with a dynamic viscosity of 1 mPa s.

226

227

228

229

230
<p align="center">**Table 2** Material properties of orthotropic materials in the model</p>

Components	Parameter	Low-frequency model	High-frequency model
Tectorial membrane	Young's modulus [Pa]	E_{XX}: 4e3 E_{YY}: 4e4 E_{ZZ}: 4e4	E_{XX}: 1.2e5 E_{YY}: 4.8e6 E_{ZZ}: 4.8e6
	Shear modulus [Pa]	G_{XY}: 2e3 G_{YZ}: 2e4 G_{XZ}: 2e3	G_{XY}: 6e4 G_{YZ}: 2.4e6 G_{XZ}: 6e4
	Poisson's ratio	$V_{XY}: \frac{1}{10}\left(\frac{1}{2}-\frac{E_{YY}}{6K}\right)$ $V_{YZ}: \frac{1}{10}\left(\frac{1}{2}-\frac{E_{YY}}{6K}\right)$ $V_{XZ}: \frac{1}{2}-\frac{E_{YY}}{6K}$	$V_{XY}: \frac{1}{40}\left(\frac{1}{2}-\frac{E_{YY}}{6K}\right)$ $V_{YZ}: \frac{1}{40}\left(\frac{1}{2}-\frac{E_{YY}}{6K}\right)$ $V_{XZ}: \frac{1}{2}-\frac{E_{YY}}{6K}$
Reticular lamina	Young's modulus [Pa]	E_{XX}: 3e8 E_{YY}: 3e9 E_{ZZ}: 3e9	E_{XX}: 9e9 E_{YY}: 3.6e11 E_{ZZ}: 3.6e11
	Shear modulus [Pa]	G_{XY}: 1e8 G_{YZ}: 1e9 G_{XZ}: 1e8	G_{XY}: 3e9 G_{YZ}: 1.2e11 G_{XZ}: 3e9
	Poisson's ratio	$V_{XY}: \frac{1}{10}\left(\frac{1}{2}-\frac{E_{YY}}{6K}\right)$ $V_{YZ}: \frac{1}{10}\left(\frac{1}{2}-\frac{E_{YY}}{6K}\right)$ $V_{XZ}: \frac{1}{2}-\frac{E_{YY}}{6K}$	$V_{XY}: \frac{1}{40}\left(\frac{1}{2}-\frac{E_{YY}}{6K}\right)$ $V_{YZ}: \frac{1}{40}\left(\frac{1}{2}-\frac{E_{YY}}{6K}\right)$ $V_{XZ}: \frac{1}{2}-\frac{E_{YY}}{6K}$
Basilar membrane	Young's modulus [Pa]	E_{XX}: 6e5 E_{YY}: 6e6 E_{ZZ}: 6e6	E_{XX}: 1.8e7 E_{YY}: 7.2e8 E_{ZZ}: 7.2e8
	Shear modulus [Pa]	G_{XY}: 2e5 G_{YZ}: 2e6 G_{XZ}: 2e5	G_{XY}: 6e6 G_{YZ}: 2.4e8 G_{XZ}: 6e6
	Poisson's ratio	$V_{XY}: \frac{1}{10}\left(\frac{1}{2}-\frac{E_{YY}}{6K}\right)$ $V_{YZ}: \frac{1}{10}\left(\frac{1}{2}-\frac{E_{YY}}{6K}\right)$ $V_{XZ}: \frac{1}{2}-\frac{E_{YY}}{6K}$	$V_{XY}: \frac{1}{40}\left(\frac{1}{2}-\frac{E_{YY}}{6K}\right)$ $V_{YZ}: \frac{1}{40}\left(\frac{1}{2}-\frac{E_{YY}}{6K}\right)$ $V_{XZ}: \frac{1}{2}-\frac{E_{YY}}{6K}$

231

232

Table 3 Material properties of isotropic materials in the model

Components	Low-frequency model Young's modulus [Pa]	High-frequency model Young's modulus [Pa]
Spiral ligament	1e9	1.2e11
Spiral lamina	1e9	1.2e11
Spiral limbus	1e6	1.2e8
Inner sulcus cell	3e3	3.6e5
Hensen stripe	3e3	3.6e5
Hensen cell	3e3	3.6e5
Deters cell	3e3	3.6e5
Deiters cell rod	1e8	1.2e10
Pillar cell head	1e7	1.2e9
Outer pillar cell	1e8	1.2e10
Inner pillar cell	1e8	1.2e10
Inner hair cell	3e3	3.6e5
Outer hair cells	1e4	1.2e6
Stereocilia	1e5	1.2e7
Phalangeal processes	1e8	1.2e10

234 **2.4 Mesh**

235 The organ of Corti includes complex three-dimensional structures. The mesh of the
236 model was adjusted to ensure the quality of the elements, as shown in Figure 1. One-
237 dimensional beam elements were used for the stereocilia, phalangeal processes, and
238 Deiters rods. All other structures were meshed with tetrahedron elements. The organ of
239 Corti and the fluid area nearby were meshed densely, and the SV, SM, and ST areas
240 were meshed relatively loosely. The low-frequency model had 36,123 solid elements,
241 184 beam elements, and 39,106 fluid elements. The high-frequency model had 34,572
242 solid elements, 171 beam elements, and 38,292 fluid elements. The quadratic elements
243 were selected for solid and fluid. The axial displacement and twist are represented by
244 linear shape functions in the beam elements, while a cubic shape function represents
245 the bending.

2.5 Stimulation of active response

The active response was calculated by superimposing acoustic and OHCs excitations to simulate the movement of the organ of Corti in the living cochlea. First, a sinusoidal pressure difference was uniformly applied to the BM to simulate the excitation when the sound propagates along the cochlea. Under the action of acoustic excitation, RL and TM will undergo shearing motion, which determines the magnitude of the load at both ends of the OHCs. The OHC force was calculated as follow (Geleoc et al., 1997; Murakoshi et al., 2015)

$$F_{OHC}(x) = \frac{F_{max}}{1+e^{\alpha_1(x_1-x)}(1+e^{\alpha_2(x_2-x)})} \tag{7}$$

where F_{max} is the maximum load that can be generated at both ends of the OHC, set to 155 nN, x is the shear displacement of RL and TM, x_1 and x_2 are the displacements, at which the setpoints of transition between states were set to 0.092 nm^{-1} and 0.038 nm^{-1}. α_1 and α_2 are the displacement sensitivities of the transitions, set to 8.2 nm and 49 nm (Geleoc et al., 1997).

3   Results

3.1 Hotspots in OHCs and DCs area

First, we calculated the active response of the organ of Corti based on the high- and low-frequency model, as shown in Figure 2. When the BM moves towards the ST, the shearing movement between the RL and TM causes OHCs to elongate. The location with the most significant response is close to OHCs and DCs, as observed in the experiments (Cooper et al., 2018).

As shown in Figure 3, a path was defined, similar to the definition in the experiment (Cooper et al., 2018), to compare the model results with the experiment. This path starts from the BM, passes through the DCs and OHCs area, and extends to the bottom of the RL. The intersection between OHCs and Deiters cells that the path passes through connects PhPs. The longitudinal displacement amplitude was calculated along the defined path using the two models, as shown in Figure 4. It can be seen that the longitudinal displacement amplitude of the two models reaches the maximum near the

273   junction of DCs and OHCs, while the response close to BM and RL is small.

274   Furthermore, the phase of DCs and OHCs is different from BM, consistent with the

275   measured results in the experiment. Our model demonstrates how hotspot vibrations

276   could be observed in the low-frequency region. It can be seen that the response

277   amplitude of the low-frequency model is greater than that of the high-frequency model

278   when driven by the same stimuli.

279
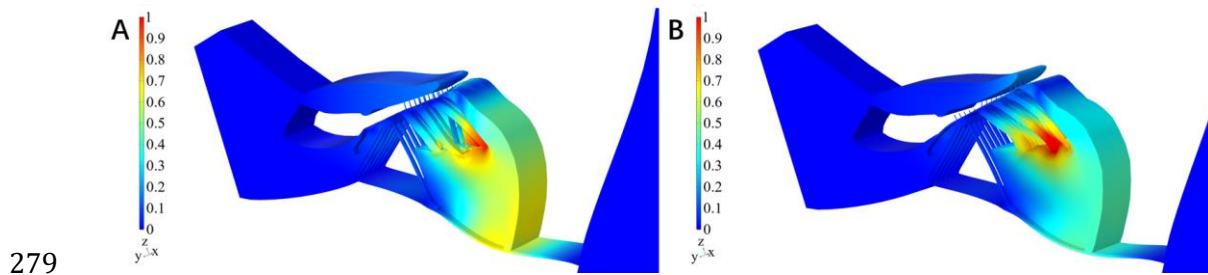
280   Figure 2: The active responses calculated based on (A) the high-frequency model and (B) the low-
281   frequency model. The amplitudes were normalized with respect to the maximum value, and the
282   deformation was magnified by 300 and 5 times for better visualization.

283
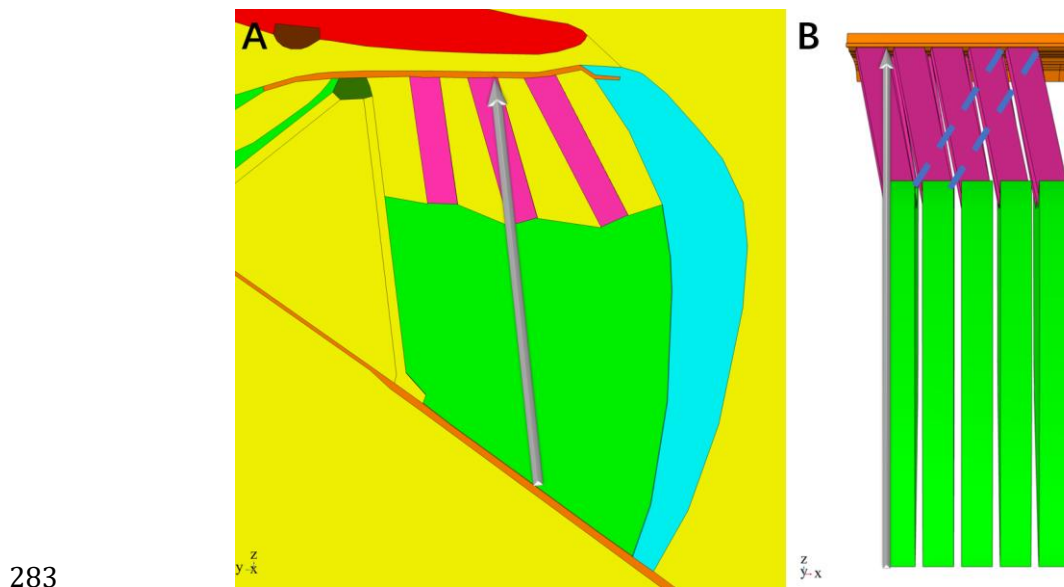
284   Figure 3: Defined path, marked with a gray arrow, for calculating longitudinal displacements of different
285   components in the organ of Corti. (A) Transverse view. (B) Longitudinal view.
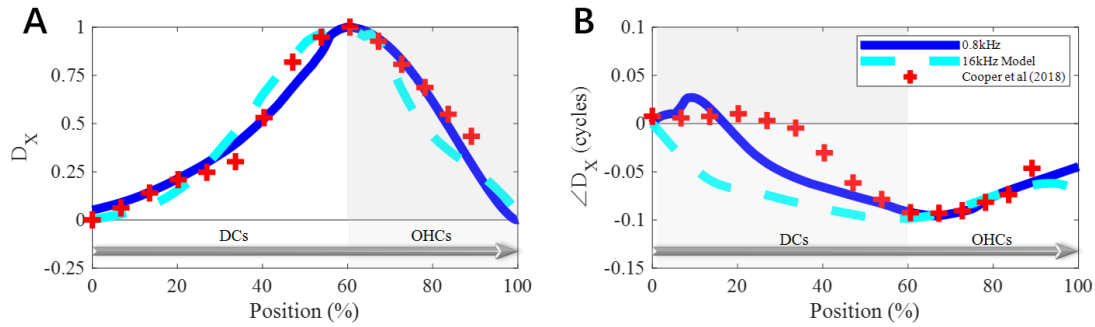
Figure 4: (A) The amplitude (A) and phase (B) of longitudinal displacement along the defined path. The amplitudes were processed with the min-max normalization method. The horizontal axis shows the percentage of the distance along the defined path.

3.2 The effect of viewing angle on the hotspot

In the experimental study, the effect of different viewing angles on the results was predicted (Cooper et al., 2018). Based on the possible complex motion of the BM, Cooper et al. speculated: "Under the effect of the traveling wave, the phase of the hotspot will lead the BM when observing towards the apex and lag the BM when observing towards the base." They then observed a similar phenomenon in their experiments.

Based on the high-frequency model, we also explored the influence of viewing angles on the hotspot. Referring to the method of Cooper et al. (2018), the viewing angle toward the cochlear apex was defined as "negative", and toward the base as "positive", as shown in Figure 5. Along with the two viewing angles, the calculated results of different deviation angles are shown in Figure 6. It can be seen that under the positive viewing angle, the results are in good agreement with the experimental results, and the hotspot phase lags to the BM. A similar phenomenon is also shown from the negative viewing angle, but the hotspot phase leads to the BM. Although the segmental model used in this study cannot include the effect of the traveling wave, the hotspot phase leading or lagging to the BM is still observed at different viewing angles. In this way, our results confirmed Cooper et al. predictions（4）and (5) (See supplementary information in Cooper et al. 2018). Since the deviation from different angles has little effect on the results, the resulst below focus on calculating the properties of the hotspot response using the positive viewing angle (specifically at $\alpha=0$).

311
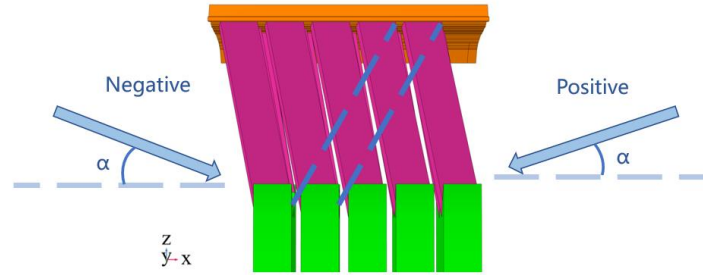
Figure 5: Sketch of different viewing angles to the longitudinal direction.
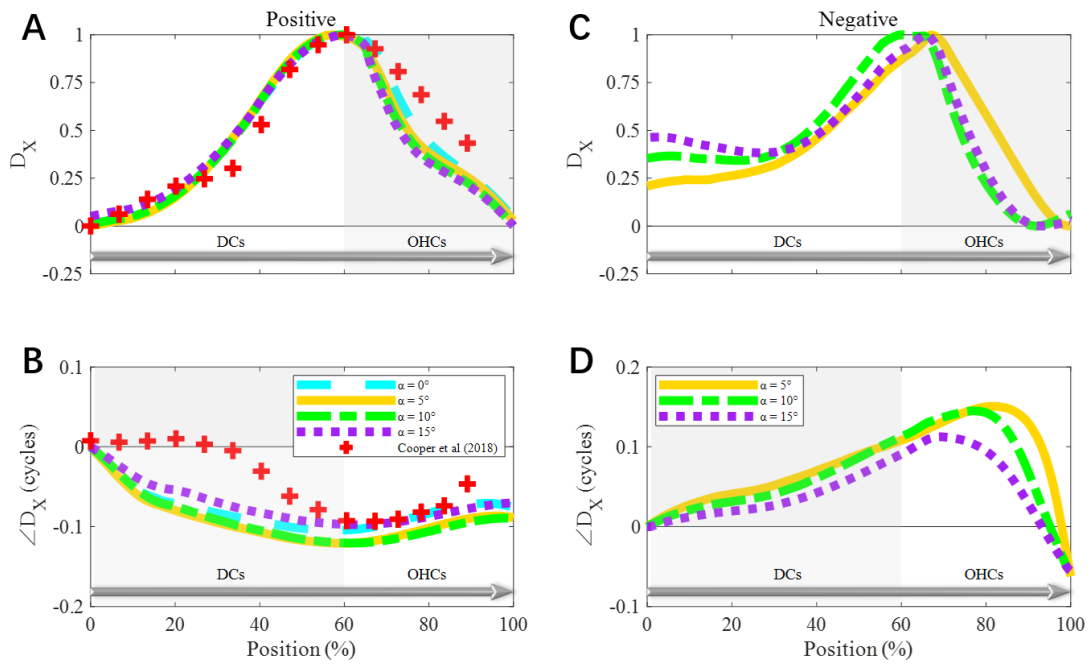
313

314 Figure 6: The positive (A, B) and negative (C, D) viewing angles, the amplitude (A, C), and phase (B,
315 D) of longitudinal displacement along the defined path. The amplitudes were processed with the min-
316 max normalization method. The phase results are calculated with reference to the position closest to the
317 BM. The horizontal axis shows the percentage of the distance along the defined path.

318 **3.3 Contributions of OHCs somatic motion and PhPs constraints to the hotspot**

319 The experimental hypothesis is that the hotspot response is triggered by the activity of
320 OHCs and is related to integrated structural constraints (Cooper et al., 2018). We
321 recalculated the movement of the organ of Corti when PhPs or OHCs excitation was
322 excluded, as shown in Figure 7. It can be seen that when the excitation of OHCs is
323 stopped, the longitudinal deformation will disappear. When the PhPs are neglected,
324 hotspot response amplitude is slightly decreased. It can be seen that the OHCs activity
325 play an essential role in producing hotspot, and the existence of PhPs has further

326   promoted the occurrence of this phenomenon.
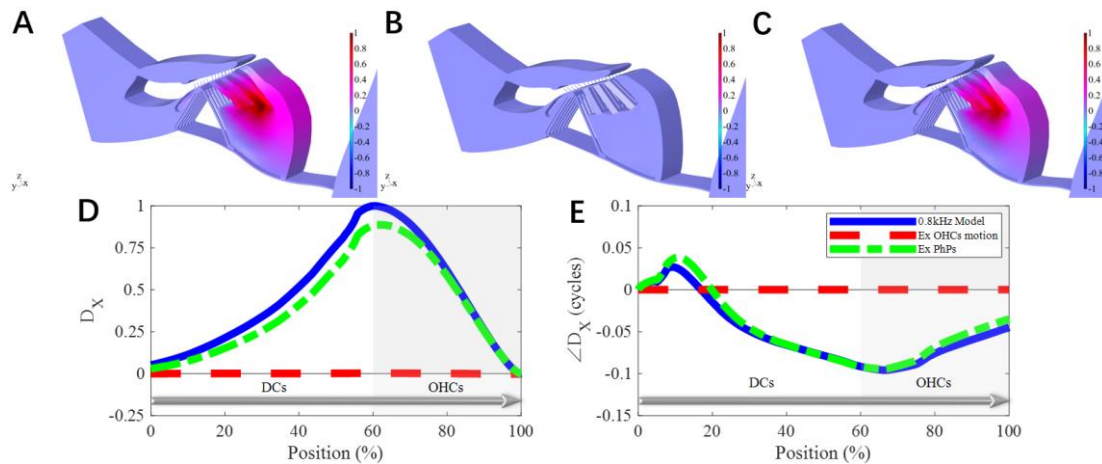
328   Figure 7: Deformation when (A) the model is fully active, (B) OHCs motility is excluded, and (C) PhPs
329   are eliminated. The longitudinal displacements in (A), (B), and (C) are normalized, and the deformation
330   is magnified 5 times (A, C) and 100 times (B) for better visualization. The amplitudes were processed
331   with the min-max normalization method.   The (D) amplitude and (E) phase of DCs and OHCs
332   longitudinal displacement. The amplitudes were normalized with respect to the results of the 0.8 kHz
333   model. The horizontal axis shows the percentage of the distance along the defined path.

3.4 The effect of OHCs tilt angle on the hotspot

335   In our model, the OHCs are inclined 10˚ in the longitudinal direction. Existing studies
336   have shown that the inclination angle of OHCs in different species is different. For
337   example, the average inclination angle of gerbils is 5˚, and that of chinchilla is 15˚
338   (Yoon et al., 2011). It was also shown that even in the same species, the tilt angles at
339   different positions of the cochlea are different. For example, the tilt range in mice is
340   from 5˚ to 15˚ (Soons et al., 2015). Moreover, some results showed that OHCs and RL
341   occasionally tend to be perpendicular (Raphael et al., 1991; Soons et al., 2015).

342   To explore the influence of different tilt angles on the hotspot response, we changed
343   the OHCs to be inclined 0˚, 5˚, 10˚, and 15˚ longitudinally, as shown in Figure 8. The
344   greater the tilt angle of the OHCs along the longitudinal direction, the greater hotspot
345   amplitude. It is worth noting that when the OHCs are not tilted in the longitudinal
346   direction, the result also shows evident hotspot vibration. This may indicate that PhPs
347   played a more critical role in this phenomenon.

348
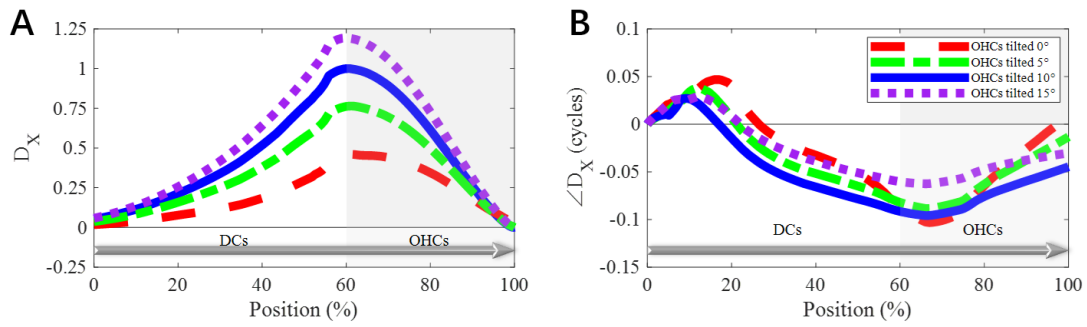
Figure 8: The amplitude (A) and phase (B) of DCs and OHCs longitudinal displacement when OHCs are inclined at different angles in the longitudinal direction. The amplitudes were normalized with respect to results when OHCs tilt 10 °. The horizontal axis shows the percentage of the distance along the defined path.

We also explored the role of PhPs on hotspots when the OHCs inclined at different angles, as shown in Figure 9. If there were no PhPs, hotspot vibration will still occur when OHCs are tilted longitudinally, even if the tilt angle is slight. But when the OHCs are not inclined in the longitudinal direction, the hotspot will disappear without PhPs.

357
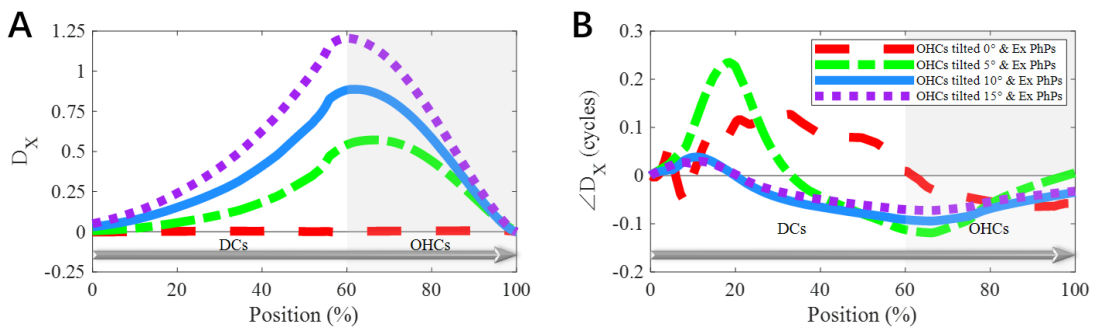
Figure 9: The amplitude (A) and (B) phase of DCs and OHCs longitudinal displacement when PhPs are excluded and OHCs inclined at different angles in the longitudinal direction. The amplitudes were normalized with respect to results when the OHCs tilted 10 °. The horizontal axis shows the percentage of the distance along the defined path.

3.5 The effect of PhPs longitudinal span on the hotspot

We first compared the hotspot responses of the high- and low-frequency models with the same PhPs span, 3 OHCs, as shown in Figure 10. It can be seen that the response amplitude of the low-frequency model is much greater than that of the high-frequency model.
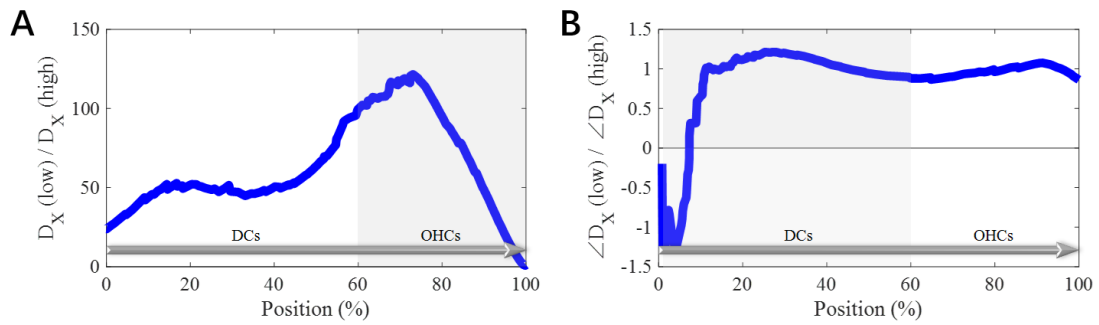
Figure 10: Comparison of DCs and OHCs (A) longitudinal displacement and (B) phase calculated with the low- and high-frequency models. The horizontal axis shows the percentage of the distance along the defined path.

Existing studies have observed geometric parameters in different species and found some differences. For example, the longitudinal span of PhPs is 2 OHCs spacing in gerbils (Karavitaki and Mountain, 2007), 3 in mouse (Soons et al., 2015), and 4-5 in mole rat (Raphael et al., 1991). Moreover, the longitudinal spacing of OHCs in these species is close, with a distance of about 10 μm. Therefore, we used the guinea pig model to study the effect of different longitudinal spans of PhPs on the hotspot response, as shown in Figure 11. It can be seen that the hotspot response is more significant when the PhPs span is shorter.
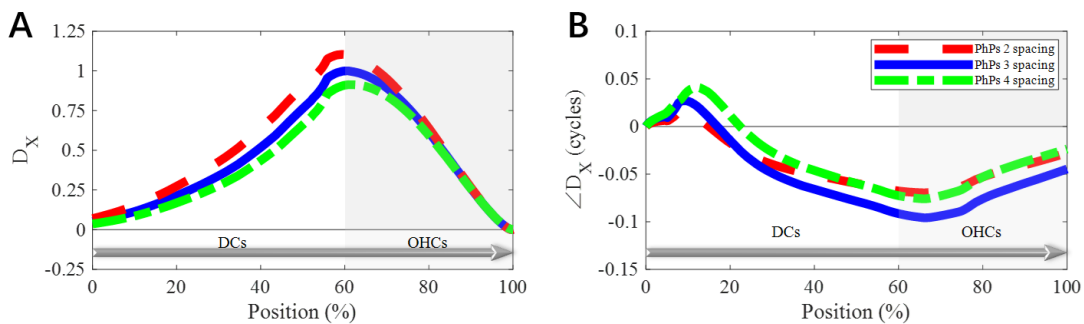
Figure 11: The amplitude (A) and phase (B) of DCs and OHCs longitudinal displacement when PhPs span different spacing along the longitudinal direction. The amplitudes were normalized with respect to results when PhPs span 3 OHCs. The horizontal axis shows the percentage of the distance along the defined path.

4 Conclusion and discussion

Two three-dimensional models of the organ of Corti were developed, describing the high- and low- frequencies regions in the cochlea, which are not a simple spatial

387 stretching but included several different continuity conditions based on the natural
388 physiological structure. Although the model constructed using beam elements could
389 reduce the amount of calculation, it cannot describe the local response of the organ of
390 Corti in detail. A three-dimensional model allows the simulation of the integrated
391 spatial coupling between solid and fluid. Compared with the two-dimensional model,
392 the three-dimensional model considers the longitudinal tilt of OHCs and the structure
393 of PhPs, which makes it possible to study the influence of these factors on the hotspot
394 phenomenon.

395 It should be noted that even without the traveling wave, our model still validated the
396 predictions (4) and (5) mentioned above and reproduced similar phenomena to
397 experiments, including the vibrational morphology of the hotspot and phase lead or lag
398 depending on the viewing angle. Therefore, we hypothesize that the hotspot is a locally
399 originated phenomenon in the cochlea, but the traveling wave further enhances the
400 response of the hotspot to low-frequency excitation.

401 When the OHCs activity was excluded, the longitudinal deformation of the OHCs and
402 DCs area was significantly reduced, confirming that the activity of OHCs induces the
403 hotspot vibration (Dewey et al., 2021). In addition, the results show that the longitudinal
404 structural constraints of PhPs also slightly contribute to the formation of the hotspot.
405 Our results confirm that the hotspot occurs in both high-frequency and low-frequency
406 regions.

407 In summary, the movement of OHCs triggers the hotspot and the PhPs structural
408 constraints promote this phenomenon, which supports the experimental hypothesis
409 (Cooper et al., 2018). The hotspot phenomenon occurs regardless of the tilt angle of the
410 OHCs, a larger tilt angle induces a larger amplitude. When OHCs are not inclined, the
411 structural constraints of PhPs become the main reason and a shorter PhPs span will
412 induce a larger hotspot amplitude.

Appendix I: Effects of Periodic Condition

Periodic conditions were assumed along the longitudinal solid side boundaries. To verify the effect of periodic conditions on the hotspot response, we extended the existing model longitudinally to 60 μm, 180 μm, 300 μm, and 420 μm, that is, the original model extended the same length along both sides of the longitudinal direction, as shown in Figure I.A, and recalculated the movement of the organ of Corti. It can be seen from Figure I.B that the movement of the organ of Corti has not changed after the model is extended. Figures I.C and D show no change in the hotspot response after the model is extended.
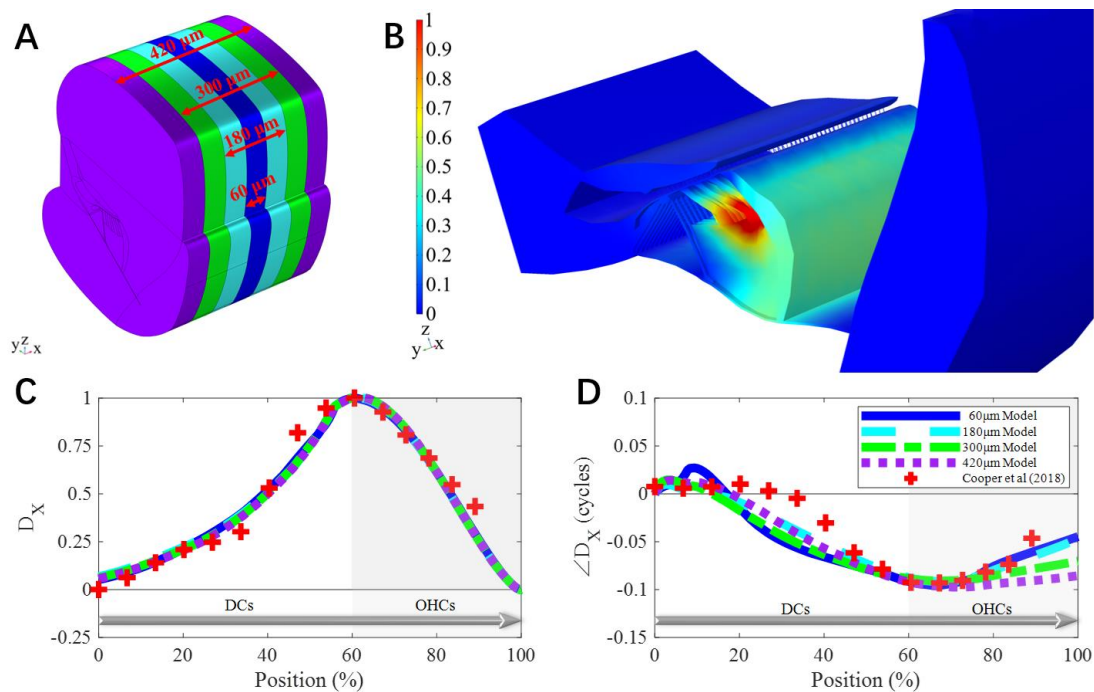
Figure I: (A) Models with different lengths in the longitudinal direction. The blue denotes 60 μm long (the original length), red 180 μm, green 300 μm, and purple 420 μm. (B) The active response of the organ of Corti when the model was extended to 420 μm. The amplitudes were processed with the min-max normalization method. The amplitude (C) and phase (D) of DCs and OHCs longitudinal displacement when the model is extended with different lengths. The amplitudes were normalized with respect to results when the model was 60 μm thick in the longitudinal direction. The horizontal axis shows the percentage of the distance along the defined path.

Appendix II: Effects of no-stress condition

The two sides of the fluid area along the longitudinal direction of the model were set as no stress conditions. Under the existing model settings, loads of different frequencies are applied to the bottom of the BM. The movement of the BM is shown in Figure II. The result showed a steady upward trend from low to high frequency, reaching the maximum value at 0.8 kHz, and rapidly decreasing. The model can simulate the response trend in the cochlea. But when the no-stress condition is eliminated, this trend does not appear.
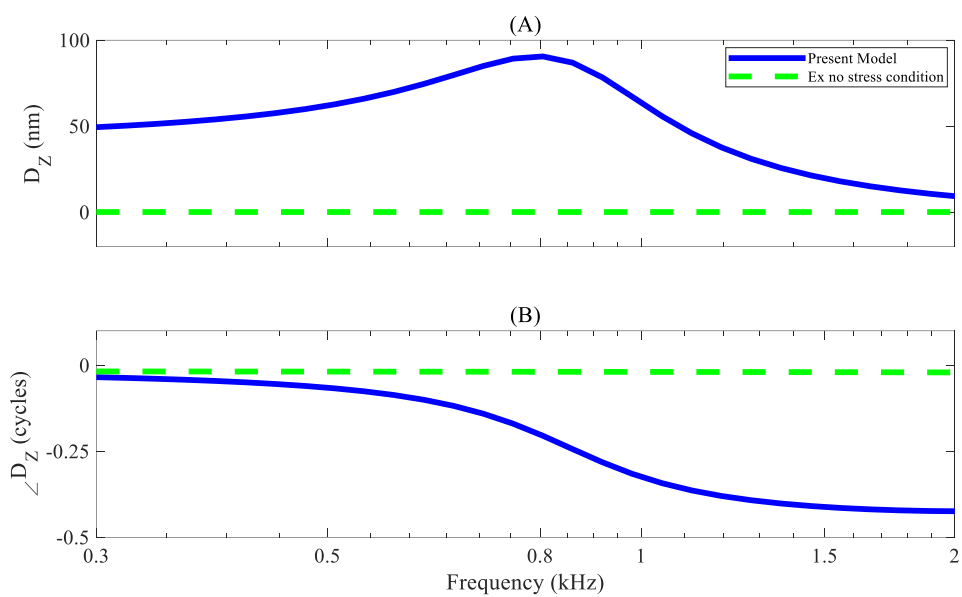
Figure II: (A) Amplitude and (B) phase of the BM vertical displacement with and without no-stress conditions.

Author Contributions

GN, JL, YB, and SJE contributed to the conception and design of the work, drafting and revising the manuscript. JL, GN, YB, QC, and SZ participated in modeling work. All authors agreed to submit the manuscript in its current state and agree to be accountable for all aspects of the work.

Acknowledgments

[1] Alec Salt's laboratory: http://oto2.wustl.edu/cochlea/ (Last viewed June 4, 2016).

References

Bohnke, F., von Mikusch-Buchberg, J., Arnold, W., 1999. Active nonlinear mechanics of the organ of Corti including the stereocilia-tectorial membrane complex. Orl-Journal for Oto-Rhino-Laryngology and Its Related Specialties 61(5), 311-317. https://doi.org/10.1159/000027689.

Cai, H.X., Chadwick, R., 2003. Radial structure of traveling waves in the inner ear. Siam Journal on Applied Mathematics 63(4), 1105-1120, Pii s0036139901388957. https://doi.org/10.1137/s0036139901388957.

Cai, H.X., Shoelson, B., Chadwick, R.S., 2004. Evidence of tectorial membrane radial motion in a propagating mode of a complex cochlear model. Proceedings of the National Academy of Sciences of the United States of America 101(16), 6243-6248. https://doi.org/10.1073/pnas.0401395101.

Cooper, N.P., Vavakou, A., van der Heijden, M., 2018. Vibration hotspots reveal longitudinal funneling of sound-evoked motion in the mammalian cochlea. Nature Communications 9, 12, 3054. https://doi.org/10.1038/s41467-018-05483-z.

Dewey, J.B., Altoe, A., Shera, C.A., Applegate, B.E., Oghalai, J.S., 2021. Cochlear outer hair cell electromotility enhances organ of Corti motion on a cycle-by-cycle basis at high frequencies in vivo. Proceedings of the National Academy of Sciences of the United States of America 118(43), e2025206118. https://doi.org/10.1073/pnas.2025206118/-/DCSupplemental.

Fallah, E., Strimbu, C.E., Olson, E.S., 2021. Nonlinearity of intracochlear motion and 442 local cochlear microphonic: Comparison between guinea pig and gerbil. Hearing 443 Research 405, 108234. https://doi.org/10.1016/j.heares.2021.108234.

Fernandez, C., 1952. DIMENSIONS OF THE COCHLEA (GUINEA PIG). Journal of the Acoustical Society of America 24(5), 519-523. https://doi.org/10.1121/1.1906929.

Geisler, C.D., Sang, C., 1995. A cochlear model using feed-forward outer-hair-cell forces. Hearing Research 86(1-2), 132-146. https://doi.org/10.1016/0378-5955(95)00064-b.

Geleoc, G.S., Lennan, G.W., Richardson, G.P., Kros, C.J., 1997. A quantitative comparison of mechanoelectrical transduction in vestibular and auditory hair cells of neonatal mice. Proceedings. Biological sciences 264(1381), 611-621. https://doi.org/10.1098/rspb.1997.0087.

Greenwood, D.D., 1990. A cochlear frequency-position function for several species--29 years later. The Journal of the Acoustical Society of America 87(6), 2592-2605. https://doi.org/10.1121/1.399052.

He, W.X., Kemp, D., Ren, T.Y., 2018. Timing of the reticular lamina and basilar membrane vibration in living gerbil cochleae. Elife 7, 17, e37625. https://doi.org/10.7554/eLife.37625.

Karavitaki, K.D., Mountain, D.C., 2007. Imaging electrically evoked micromechanical motion within the organ of corti of the excised gerbil cochlea. Biophysical Journal 92(9), 3294-3316. https://doi.org/10.1529/biophysj.106.083634.

Kelly, J.P., 1989. Cellular organization of the guinea pig's cochlea. Acta oto-laryngologica. Supplementum 467, 97-112.

Kikuchi, T., Kimura, R.S., Paul, D.L., Adams, J.C., 1995. Gap junctions in the rat cochlea: immunohistochemical and ultrastructural analysis. Anatomy and embryology 191(2), 101-118. https://doi.org/10.1007/bf00186783.

Lim, D.J., 1986. FUNCTIONAL STRUCTURE OF THE ORGAN OF CORTI - A REVIEW. Hearing Research 22(1-3), 117-146. https://doi.org/10.1016/0378-5955(86)90089-4.

Liu, S., White, R.D., 2008. Orthotropic material properties of the gerbil basilar membrane. Journal of the Acoustical Society of America 123(4), 2160-2171. https://doi.org/10.1121/1.2871682.

Muller, M., 1996. The cochlear place-frequency map of the adult and developing Mongolian gerbil. Hearing Research 94(1-2), 148-156. https://doi.org/10.1016/0378-5955(95)00230-8.

Murakoshi, M., Suzuki, S., Wada, H., 2015. All Three Rows of Outer Hair Cells Are Required for Cochlear Amplification. Biomed Research International 2015, 12, 727434. https://doi.org/10.1155/2015/727434.

Nam, J.-H., 2014. Microstructures in the Organ of Corti Help Outer Hair Cells Form Traveling Waves along the Cochlear Coil. Biophysical journal 106(11), 2426-2433. https://doi.org/10.1016/j.bpj.2014.04.018.

Nam, J.-H., Fettiplace, R., 2010. Force Transmission in the Organ of Corti Micromachine. Biophysical journal 98(12), 2813-2821. https://doi.org/10.1016/j.bpj.2010.03.052.

Ni, G., Elliott, S.J., 2013. Effect of basilar membrane radial velocity profile on fluid coupling in the cochlea. Journal of the Acoustical Society of America 133(3), EL181-EL187. https://doi.org/10.1121/1.4789863.

Ni, G., Elliott, S.J., Baumgart, J., 2016. Finite-element model of the active organ of Corti. Journal of the Royal Society Interface 13(115), 20150913. https://doi.org/10.1098/rsif.2015.0913.

523 Ni, G.J., Sun, L.Y., Elliott, S.J., 2017. A linearly tapered box model of the cochlea.
524 Journal of the Acoustical Society of America 141(3), 1793-1803.
525 https://doi.org/10.1121/1.4977750.

526 Nuttall, A.L., Guo, M.H., Ren, T.Y., 1999. The radial pattern of basilar membrane
527 motion evoked by electric stimulation of the cochlea. Hearing Research 131(1-2), 39-
528 46. https://doi.org/10.1016/s0378-5955(99)00009-x.

529 Raphael, Y., Altschuler, R.A., 2003. Structure and innervation of the cochlea. Brain
530 Research Bulletin 60(5-6), 397-422. https://doi.org/10.1016/s0361-9230(03)00047-9.

531 Raphael, Y., Lenoir, M., Wroblewski, R., Pujol, R., 1991. The sensory epithelium and
532 its innervation in the mole rat cochlea. The Journal of comparative neurology 314(2),
533 367-382. https://doi.org/10.1002/cne.903140211.

534 Ren, T.Y., He, W.X., Kemp, D., 2016. Reticular lamina and basilar membrane
535 vibrations in living mouse cochleae. Proceedings of the National Academy of Sciences
536 of the United States of America 113(35), 9910-9915.
537 https://doi.org/10.1073/pnas.1607428113.

538 Robles, L., Ruggero, M.A., 2001. Mechanics of the mammalian cochlea. Physiological
539 Reviews 81(3), 1305-1352.

540 Soons, J.A.M., Ricci, A.J., Steele, C.R., Puria, S., 2015. Cytoarchitecture of the Mouse
541 Organ of Corti from Base to Apex, Determined Using In Situ Two-Photon Imaging.
542 Jaro-Journal of the Association for Research in Otolaryngology 16(1), 47-66.
543 https://doi.org/10.1007/s10162-014-0497-1.

544 Steele, C.R., Baker, G., Tolomeo, J., Zetes, D., 1993. Electro-mechanical models of the
545 outer hair cell.

546 Steele, C.R., Lim, K.M., 1999. Cochlear model with three-dimensional fluid, inner
547 sulcus and feed-forward mechanism. Audiology and Neuro-Otology 4(3-4), 197-203.
548 https://doi.org/10.1159/000013841.

549 Steele, C.R., Puria, S., 2005. Force on inner hair cell cilia. International Journal of
550 Solids and Structures 42(21-22), 5887-5904.
551 https://doi.org/10.1016/j.ijsolstr.2005.03.056.

552 von Bekesy, G., 1970. Travelling waves as frequency analysers in the cochlea. Nature
553 225(5239), 1207-1209. https://doi.org/10.1038/2251207a0.

554 Yoon, Y.J., Steele, C.R., Puria, S., 2011. Feed-Forward and Feed-Backward
555 Amplification Model from Cochlear Cytoarchitecture: An Interspecies Comparison.
556 Biophysical journal 100(1), 1-10. https://doi.org/10.1016/j.bpj.2010.11.039.

557 Zagadou, B.F., Barbone, P.E., Mountain, D.C., 2020. Significance of the Microfluidic
558 Flow Inside the Organ of Corti. Journal of Biomechanical Engineering-Transactions of
559 the Asme 142(8), 12, 081009. https://doi.org/10.1115/1.4046637.

560 Zetes, D.E., Tolomeo, J.A., Holley, M.C., 2012. Structure and Mechanics of Supporting
561 Cells in the Guinea Pig Organ of Corti. Plos One 7(11), e49338.
562 https://doi.org/10.1371/journal.pone.0049338.

563 Zwislocki, J.J., Cefaratti, L.K., 1989. Tectorial membrane II: Stiffness measurements
564 in vivo. Hearing Research 42(2), 211-227. https://doi.org/https://doi.org/10.1016/0378-
565 5955(89)90146-9.

566